Sensors & Actuators: B. Chemical 403 (2024) 135134



Contents lists available at ScienceDirect

Sensors and Actuators: B. Chemical

journal homepage: www.elsevier.com/locate/snb





Tailoring titanosilicate molecular sieves by vanadium substitution for humidity sensing applications

Ramona Davoudnezhad [a,*], Duygu Kuzyaka [a,c], Burcu Akata [a,b,**]

[a] Micro and Nanotechnology Program, Middle East Technical University, Ankara 06800, Turkey
[b] Central Laboratory, Middle East Technical University, Ankara 06800, Turkey
[c] Center for Solar Energy Research and Applications (ODTÜ-GÜNAM), Middle East Technical University, Ankara 06800, Turkey

ARTICLE INFO

Keywords:
Humidity sensor
Titanosilicates
V-incorporated ETS-10
Impedance spectroscopy

ABSTRACT

There is a great interest in developing humidity sensors with enhanced sensitivity at all relative humidity (*RH*) ranges. To explore this, vanadium (V)-incorporated titanosilicate microporous thin films were successfully fabricated to investigate their performances as humidity sensors. The V-precursor was directly added to obtain V/V+Ti atomic of 0.1 ($V_{0.1}$ETS-10) to 0.2 ($V_{0.2}$ETS-10) and 0.3 ($V_{0.3}$ETS-10), and characterized by FE-SEM, XRD, Raman, UV-Vis, and XPS analyses. The ETS-10 sensor displayed high sensitivity (1.11×10^4) and linearity (R^2=0.9818) at room temperature across medium (32–67 %) and high (>67 %) relative humidity (*RH*), with rapid response (~8 s) and recovery times (~35 s). The sensor with an optimized amount of vanadium doping ($V_{0.2}$ETS-10), showed a significant improvement in the performance in the low *RH* region (8–32 %) with enhanced sensitivity (1.75×10^4) and linearity (R^2=0.9914). The results of our study indicate that the formation of Ti^{3+} with the emergence of V^{4+} and V^{5+} states resulted in enhanced sensitivity at low *RH* levels. Based on the obtained results, a plausible shift in the humidity sensing mechanism evolves from chemisorbed intracrystalline water to physisorbed intercrytalline and surface water with increasing *RH*. However, higher vanadium content led to structural alteration and impurities resulting in a notable reduction in sensitivity (1.17×10^3) and linearity (R^2=0.8927).

1. Introduction

There has been a rapid increase in developing sensors for monitoring moisture, temperature, and chemical gases in various application fields [1–3]. Humidity sensors hold an imperative role due to increased demand to control the indoor ambient environment, food and medicine storage, agriculture, health, industry, textile, and even space environments. The research in humidity sensors faces the profound challenge of sensing humidity variation in the whole humidity range from low (3–30 % *RH*) to high (>60 % *RH*) relative humidity, resulting in increased research devoted to developing new materials for humidity sensing applications [4]. The constructive design of a high-performance humidity sensor is a rather complicated topic due to various design factors, such as linear response, high sensitivity, fast response and recovery times, chemical and physical stability, wide operating humidity range, and low cost.

Tailoring active materials to enhance their sensing properties for a broader range of humidity levels presents a significant challenge in the quest to improve the performance of humidity sensors. Typically, this tailoring process involves post-synthesis treatment protocols aimed at increased surface area, number of defect sites, or optimized pore volume. These enhancements often require sophisticated synthetic schemes and synthetic conditions with dopants [5,6]. While these steps hold promise for improving sensor performance, they also entail extra fabrication steps. Notably, adding the desired dopant with different concentrations during synthesis reduces the production cost [7].

The most common sensing materials studied for humidity sensing are ceramics (non-metallics, semiconductor metal oxides, etc.), polymers, and ceramic/polymers [8,9]. Among them, titanium dioxide (TiO_2) was shown to be of particular interest due to its high response in electrical conductivity, hydrophilicity, wide resistivity range, and high chemical and thermal stability. However, reported TiO_2-based humidity sensors, with no post-synthetic modifications made to their structural composition, showed low sensitivity at a low relative humidity range [9].

* Corresponding author.
** Correspondence to: Middle East Technical University, Central Laboratory, Ankara 06800, Turkey.
E-mail addresses: Ramona.davoudnejad@gmail.com (R. Davoudnezhad), akata@metu.edu.tr (B. Akata).

https://doi.org/10.1016/j.snb.2023.135134
Received 20 June 2023; Received in revised form 5 December 2023; Accepted 8 December 2023
Available online 17 December 2023
0925-4005/© 2023 Elsevier B.V. All rights reserved.

Therefore, many efforts have been performed to improve the sensitivity of as-synthesized TiO_2, aiming to modify the structure by doping transition metals. The doping process, such as LiCl or graphene was reported to induce additional atomic defects and functional groups enhancing the sensor's electrical response [10,11]. Another example can be given by the study made by Haidry et al., reporting that humidity sensitivity can be controlled by varying Co/Ti in Co-doped TiO_2 mesoporous structures or manipulating pore size using a template as a mesoporogen with small pore sizes resulting in a high response [12,13]. Among others, vanadium oxide has been effectively used as one of the dopants leading to enhancements in different sensing mechanisms [14–18].

An opportunity to regulate the humidity sensing performance can be achieved using Ti-based molecular sieves with a high surface area and tunable defect sites readily available in their structure. Engelhard titanosilicate (ETS-10) is a microporous zeotype material that contains periodically positioned -Ti-O-Ti- chains with a diameter (*d*) of ~0.67 nm running along two orthogonal directions, surrounded by tetrahedral silicate units [19]. Among other molecular sieves, ETS-10 has been the subject of extensive research due to these quantum wires that impart some fascinating properties [19,20]. Replacing vanadium ions with titanium in the structure of ETS-10 had only been investigated for their effect on enhanced photoreactivity in the visible region until now [21, 22]. Vanadium doping was used as a tailoring method for changing the number of defects present in ETS-10, exposing more Ti/V–OH active sites and V^{5+} cations along the chains [21,22]. The defective sites created on such surfaces were also reported to have a role in water adsorption, producing a large number of conductive H_3O^+ ions [23,24]. Although the creation of defects in ETS-10 and their specific role in the humidity sensing mechanism had never been investigated before, the humidity sensing behavior is known to be a measure of the proton (H^+) conductivity tailored by the number of defective hydroxyl groups affecting the proton hopping mechanism [8,9].

This study aimed to develop humidity sensors based on thin films of titanosilicate ETS-10 and direct synthesis of V-incorporated ETS-10. To achieve this goal, vanadium precursor was directly added during the ETS-10 synthesis with varying amounts, and then the films were fabricated using synthesized samples to investigate the humidity sensing performance of the obtained sensors. The unique chemical structure of ETS-10, which features chains of one-dimensional -Ti-O-Ti- units that impart greater flexibility, was leveraged to create an increased number of defects in these materials. As a result, ETS-10 and V-incorporated ETS-10 were investigated to be novel candidates for use in humidity sensors.

2. Experimental

2.1. Synthesis of ETS-10 and vanadium-substituted ETS-10

ETS-10 crystals were synthesized using the molar formulation of $3.4Na_2O$:1.5 K_2O:TiO_2:5.5 SiO_2:180 H_2O [25]. Typically, Si precursor was prepared by dissolving sodium silicate solution (27 wt% SiO_2, 8 wt % Na_2O, and 65 wt% H_2O, Aldrich), NaCl, and KCl in deionized water. For the preparation of Ti precursor, P25 (76 wt% anatase and 24 wt% rutile, Degussa) was used as a titanium source and dissolved H_2SO_4 in deionized water in a separate bottle. The Ti precursor was then poured into the Si precursor, and the resulting mixtures were hand-shaken for 5–10 min to form a white, viscous gel which provided sufficient time for obtaining a good quality product as also applied in other ETS-10 studies [26,27].

For the preparation of V-incorporated ETS-10 samples, $VOSO_4 \cdot xH_2O$ of various amounts were added to the Ti precursor keeping all synthesis recipes the same [22]. The parent Ti precursor was modified using a vanadium amount of 0.25, 0.75, and 1.25 g for this investigation. Samples with V/(V+Ti) molar ratios of 0.1, 0.2, and 0.3, as verified by EDAX were denoted as $V_{0.1}$ETS-10, $V_{0.2}$ETS-10, and $V_{0.3}$ETS-10, respectively. The gel was then transferred into a Teflon-lined stainless-steel autoclave, and the hydrothermal synthesis was performed at 503 K for 3 days. Afterward, the samples were cooled down to room temperature, and the obtained product was extracted by centrifugation and washed with deionized water three times. Finally, the product was dried overnight at approximately 343 K in the oven.

2.2. Humidity sensor configuration

A homemade experimental setup was designed to investigate the humidity-sensing measurements of the prepared films. For this purpose, silicone masks with a finger width of 900 μm and inter-finger spacing of about 500 μm were placed on the surface of the quartz glass substrate with dimensions of 10 × 25 mm to obtain interdigitated electrodes on the substrates. Gold electrode contacts were obtained on the substrate with the help of a mask to create interdigitated electrodes under argon gas using the plasma spraying method. The pre-synthesized ETS-10 and V_xETS-10 powder samples were mixed with 7 wt% ethanol and spin-coated twice onto the gold interdigitated electrodes that were coated on glass substrates, thereby forming the humidity-sensing films. A schematic representation of the experimental setup is provided in Fig. 1. This setup was intended to provide controlled environmental conditions for evaluating the sensitivity and accuracy of humidity sensors.

The performance of the humidity sensors was measured by using the setup shown in Fig. 1. Accordingly, different humidity conditions were established using several saturated salt solutions with different relative humidity levels in the containers. Eleven saturated salt solutions containing NaOH, LiCl, CH_3CO_2K, $MgCl_2$, K_2CO_3, Mg_2NO_3, KI, NaCl, KCl, K_2NO_3, K_2SO_4 with relative humidities of 8.24 %, 11.32 %, 23.27 %, 32.78 %, 43.16 %, 52.89 %, 67.32 %, 75.29 %, 84.34 %, 93.58 %, 97.36 %, respectively were used for humidity response measurements. For testing the humidity sensing performances of the sensors, as-prepared samples were inserted into the humidity chambers connected to the Agilent 4294 A impedance analyzer. All the measurements were performed at a voltage of 500 mV and a frequency of 100 Hz-1 MHz at room temperature. The values were recorded when the relative humidity values in the chambers were stabilized at the pre-specified relative humidity level. A commercial humidity sensor (Testo 175 H1 Datalogger) was used to verify the relative humidity (*RH*) values of prepared saturated salt solution chambers for all *RH* levels. A needle probe was attached to the humidity sensor and fitted to the lid of the chambers to ensure the *RH* level of each solution.

A different measurement setup was used to evaluate the response and recovery time of the humidity sensors. This setup consisted of two chambers: a reference chamber containing room air at typical ambient conditions with a relative humidity of approximately 32 % and a second chamber filled with water at a controlled room temperature of 24°C. These chambers were interconnected via a valve, allowing a change from 32 % to 97 % relative humidity levels in real-life conditions. The sensor's output was measured by Agilent 4294 A impedance analyzer. The response time of the humidity sensor was measured by continuously monitoring its output and recording the time it took for the sensor to reach 90 % of the final value corresponding to the increased humidity level. Following the response time measurement, the valve was closed to halt the flow of water vapor. The recovery time of the humidity sensor was then determined by recording the time it took for the reading to return to 90 % of the baseline humidity level. All *RH* levels were controlled by a commercial humidity sensor.

2.3. Characterization

ETS-10 and V-incorporated ETS-10 crystals were characterized by various techniques such as Field Emission Scanning Electron Microscopy (FE-SEM), X-ray Diffraction (XRD), Energy Dispersive X-ray (EDX), Raman Spectroscopy, and X-ray Photoelectron Spectroscopy (XPS). FE-SEM images were acquired, and EDX data were collected for the samples using a Hitachi S-4700 FE-SEM (accelerating voltage 10 kV, beam current 10 μA) in the secondary electron imaging mode. XRD analysis

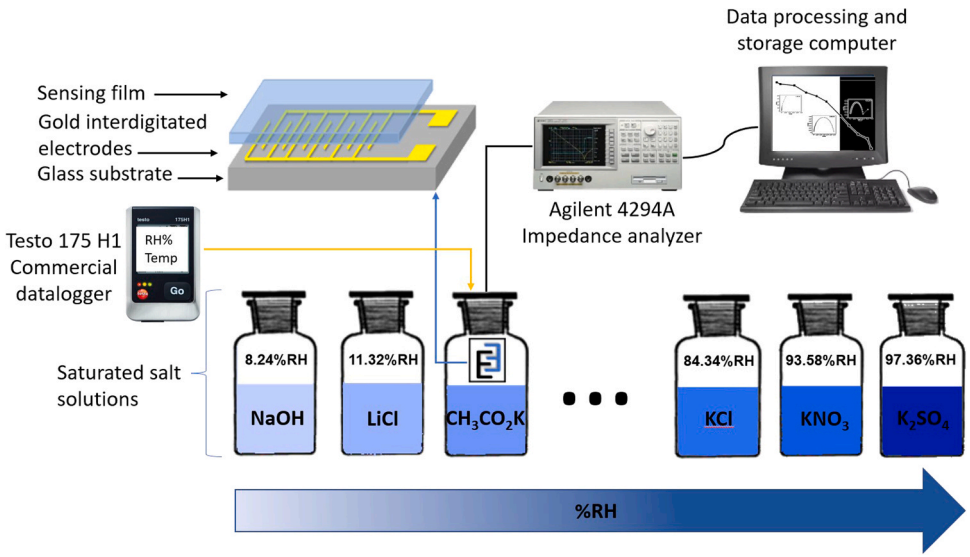


Fig. 1. Schematic of the prepared experimental setup. The system comprises chambers containing various saturated salt solutions that enable the creation of different levels of relative humidity. The sensors under evaluation are placed inside these chambers, and the entire setup is connected to an impedance analyzer. The humidity sensing performance of the sensors was assessed by varying the chambers to achieve different humidity levels, with the impedance analyzer measuring changes in the electrical properties of the sensors in response to humidity.

was carried out using Rigaku Miniflex operating at 40 kV and 15 mA with Bragg-Brentano geometry, Ni filter, and CuKα radiation. The diffraction peaks were scanned between 5° and 40°.

Renishaw-type Raman microscope was utilized in the Raman spectroscopy analyses, where the excitation wavelength of 532 nm and a power of 0.5–1 mW were chosen for the acquisition. XPS analysis was carried out on a PHI 5000 Versa Probe spectrometer with an Al-Kα radiation source. The binding energies were referenced to the internal standard C 1 s binding energy at 284.5 eV. XPS peaks are referenced to the C 1 s peak. The sub-peaks under the high-resolution vanadium, titanium, and oxygen spectra were identified by using PeakFit v4.12. Gaussian–Lorentzian functions after removal of the background by choosing a two-point linear background function.

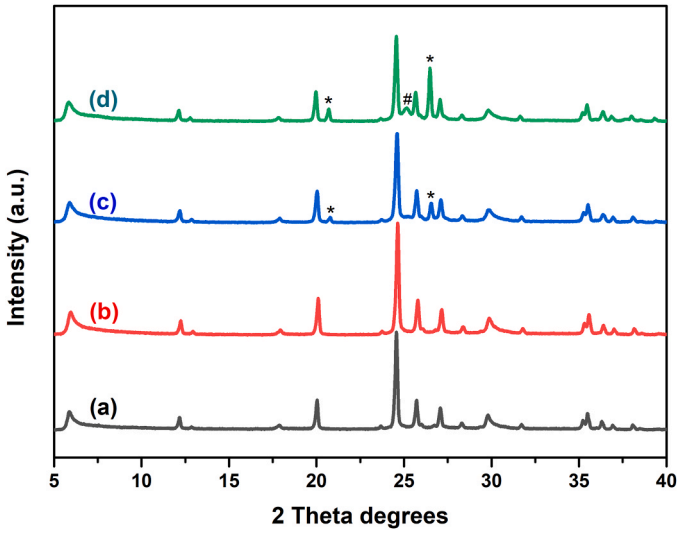


Fig. 2. XRD pattern of ETS-10 (a), $V_{0.1}$ETS-10 (b), $V_{0.2}$ETS-10 (c), $V_{0.3}$ETS-10 (d) (*quartz, #anatase) impurities.

3. Results and discussion

3.1. Sample characterization

Fig. 2 shows the XRD patterns of ETS-10 and V-incorporated V_xETS-10 samples. The XRD patterns indicate the successful synthesis of ETS-10 by adding V-containing gel in differing amounts. All samples showed good crystallinity with a small amount of impurity in $V_{0.2}$ETS-10 and $V_{0.3}$ETS-10 samples. When the amount of vanadium was increased in the synthesis gel, the amount of quartz and anatase also increased, as indicated in Fig. 2. It can be concluded that the addition of a vanadium source into the synthesis gel in differing amounts resulted in the successful formation of V-incorporated samples of ETS-10 with a more significant quartz and anatase formation as the amount of substituted vanadium increased.

The chemical composition of ETS-10 and V-incorporated ETS-10 samples is shown in Table 1. The elemental composition of the samples was found to correlate well with the expected results from the synthesis gel. Increasing vanadium content in the synthesis gel resulted in a gradual increase of vanadium content in the V_xETS-10 samples showing the successful replacement of vanadium with titanium atom. Accordingly, the total amount of V+Ti increased for higher vanadium content, resulting in a gradual decrease in Si/(V+Ti). However, this ratio increased again for sample $V_{0.3}$ETS-10, probably due to a significant increase in the silica-containing impurity, which was also observed in XRD results (Fig. 2).

The (Na+K)/(V+Ti) ratio of 1.65 ± 0.03 for the unmodified ETS-10 sample was comparable with the literature data [22]. However, this ratio decreased with the substitution of vanadium. This may be due to the presence of extra-framework sites in which the V^{4+} and V^{5+} ions would balance some of the framework charges and result in an overall decrease in the (Na + K) content. Different amounts of V^{4+} and V^{5+}

Table 1
Bulk atomic ratio of samples ETS-10, $V_{0.1}$ETS-10, $V_{0.2}$ETS-10, and $V_{0.3}$ETS-10.

Sample	V/ (V+Ti)	Si/ (V+Ti)	(Na+K)/ (V+Ti)
ETS-10	0	4.56 ± 0.02	1.65 ± 0.03
$V_{0.1}$ETS-10	0.10 ± 0.01	2.58 ± 0.06	0.99 ± 0.17
$V_{0.2}$ETS-10	0.20 ± 0.01	2.15 ± 0.11	1.10 ± 0.07
$V_{0.3}$ETS-10	0.31 ± 0.00	3.69 ± 0.12	1.21 ± 0.07

cations in the structure would cause the need for different amounts of Na^+ and K^+ ions to balance the electroneutrality of the overall structure. In addition to these, the micropore volume of the original sample may increase with the incorporation of vanadium since the sizes of V^{4+} and V^{5+} cations are slightly smaller than the Ti^{4+}ion. (i.e., 0.68 Å, 0.72 Å, and 0.75 Å for V^{5+}, V^{4+}, and Ti^{4+}, respectively) [22].

The morphologies, i.e., the crystal size of ETS-10, were shown to have an impact on the vibrational properties affecting the band gap of ETS-10 crystals [19]. The degree of crystal size was shown to correlate with the length of -Ti-O-Ti- wires, indicating a change in the degree of defect per volume of ETS-10 crystal [28]. It is known that the defects created upon breakage of the -Ti-O-Ti- wire could affect the water adsorption behavior and, thus, the humidity sensor sensitivity [15]. Accordingly, SEM analysis was performed to investigate the morphological changes induced in ETS-10 crystals upon vanadium incorporation.

Crystal size and morphological differences of ETS-10 and V_xETS-10 samples resulting from the vanadium incorporation are shown in Fig. 3.

Typical ETS-10 crystals of approximately 0.5 μm were obtained with bipyramidal morphology, as also indicated in the literature [25]. It seems that the addition of vanadium in the synthesis gel led to a slight decrease in particle size with a mixture of truncated bipyramidal and cubic-like crystals in addition to square bipyramidal morphology, as shown in Fig. 3b and Fig. 3c ($V_{0.1}$ETS-10 and $V_{0.2}$ETS-10). Further increase in vanadium content resulted in bigger crystals with a more significant formation of cubic-like morphology and larger agglomerates of possible impurities, as shown in Fig. 3d ($V_{0.3}$ETS-10). The results indicated that the addition of $VOSO_4$ as a vanadium source into the synthesis gel of ETS-10 resulted in an alteration towards a more cubic-like morphology.

Raman spectroscopy was employed to assess the quality of -Ti-O-Ti- and -V-O-V- wires [28,29]. Fig. 4 shows the Raman spectra of ETS-10 and substituted ETS-10 samples. A prominent band at approximately

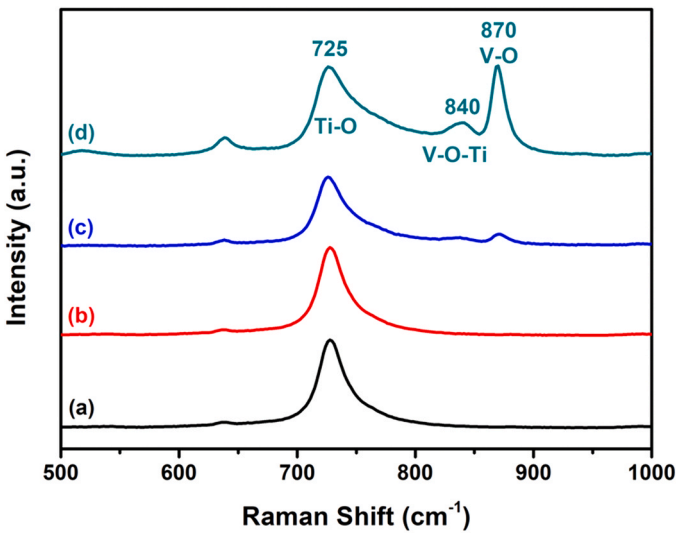


Fig. 4. Raman spectra of ETS-10, $V_{0.1}$ETVS-10, $V_{0.2}$ETVS-10, and $V_{0.3}$ETVS-10.

725 cm^{-1} is attributed to the symmetric Ti–O stretching vibration in octahedral TiO_6 units along the -Ti-O-Ti- wires. It was seen that the full-width half maximum (FWHM) of this peak broadens from 22.01 for ETS-10 to 25.7, 28.9, and 34.03 for $V_{0.1}$ETS-10, $V_{0.2}$ETS-10, and $V_{0.3}$ETS-10, respectively, indicating an increase in the vanadium content. The FWHM was reported to be around 25 cm^{-1} for a high-quality ETS-10 crystal, which broadens as the crystal deteriorates [19]. Therefore, the inclusion of vanadium appears to generate defects in these wires, along with the emergence of new bands. The Raman spectra of V-substituted V_xETS-10 samples exhibit an additional longitudinal -V-O-V- ($V^{4+}O_3^{2-}$ chains) vibration at 870 cm^{-1}, in addition to small

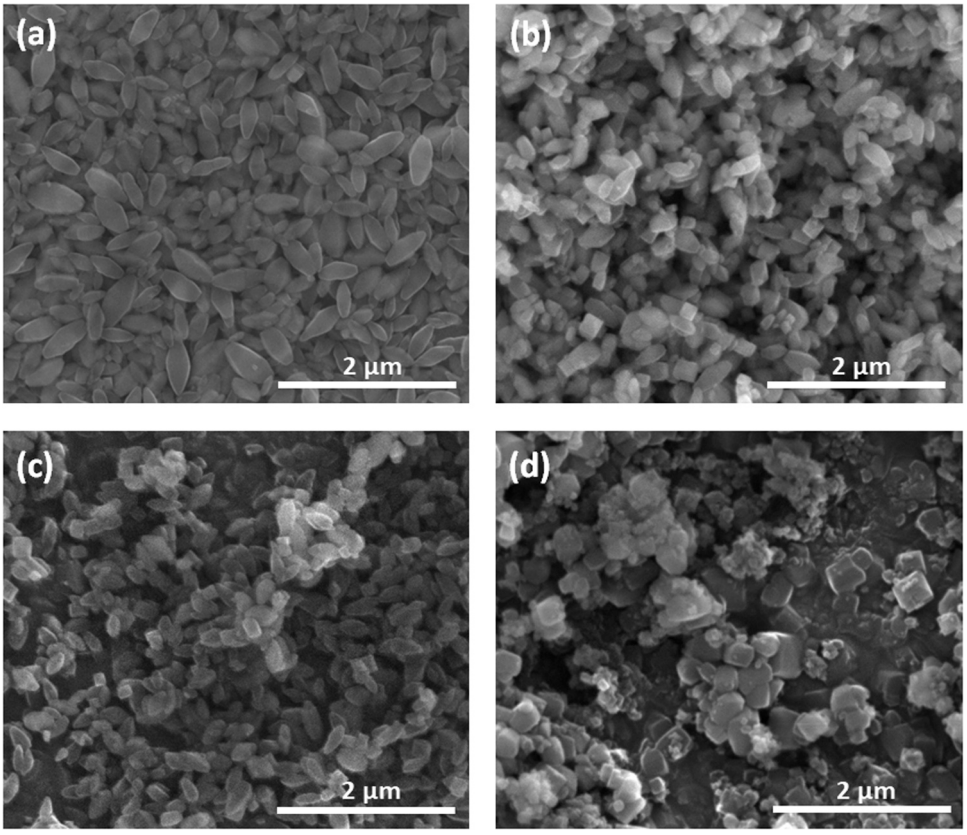


Fig. 3. SEM images of ETS-10 (a), $V_{0.1}$ETS-10 (b), $V_{0.2}$ETS-10 (c), and $V_{0.3}$ETS-10 (d).

vanadium peaks at 640 and 840 cm^{-1}. The principal band at 870 cm^{-1}, which becomes more pronounced with vanadium incorporation, is ascribed to undistorted VO_6 octahedra. The gradual broadening and decreasing intensity of 725 cm^{-1}, in conjunction with the increasing intensity of 870 cm^{-1} band, suggests the replacement of vanadium for titanium in the framework, resulting in some significant defect formation along the wires. Therefore, while $V_{0.2}$ETS-10 demonstrates some significant wire deformation with new V-O band formations, the considerably different Raman spectrum of $V_{0.3}$ETS-10 may be indicative of excessive vanadium doping in the ETS-10 structure. This behavior was also attributed to changes in the local wire environment [21,22].

To gain more understanding of the -Ti-O-Ti- wires of ETS-10 following vanadium incorporation, X-ray photoelectron spectroscopy (XPS) was utilized. It is worth noting that the factors that influence the formation of defects and the possible impact on humidity sensing performance may be linked to different oxidation states of V^{4+} and V^{5+} [22]. The introduction of vanadium and its states were shown to generate -OH groups and induce electron transfer, enhancing the adsorption ability [30].

Fig. 5 displays the XPS spectra of Ti 2p, O 1s, and V 2p of ETS-10 and vanadium-incorporated ETS-10 samples.

As depicted in Fig. 5, the XPS peaks at around 457.8 eV and 458.7 eV were assigned to Ti $2p_{3/2}$ of Ti^{3+} and Ti^{4+}, respectively [20]. A significant shift in the main peak towards the lower binding energy was observed as the amount of vanadium incorporation increased from $V_{0.1}$ETS-10 to $V_{0.2}$ETS-10 and $V_{0.3}$ETS-10, indicating a decrease in the amount of Ti^{4+} and an increase in the amount of Ti^{3+} resulting in a non-stoichiometric wire [31]. A comparable shift was observed for V-doped TiO_2, which was attributed to the increased non-stoichiometry of TiO_2 NPs toward Ti^{3+} [30]. It was also suggested that the presence of oxygen vacancies in the TiO_2 structure led to the emergence of Ti^{3+} states alongside Ti^{4+} states upon increasing vanadium incorporation levels [32]. Similar results were obtained by Liu et al. in a study of photocatalysis under vacuum conditions in V-doped TiO_2. A shift to lower binding energy in all cases indicated an increase in the electron density around Ti in doped TiO_2, attributed to the formation of Ti^{3+} [33]. The incorporation of vanadium induced structural changes in ETS-10 can be postulated to result in the formation of Ti^{3+} centers alongside Ti^{4+} states. This could possibly enhance sensitivity in the humidity sensing mechanism [14,30].

As seen in Fig. 5b, vanadium incorporation led to the O 1s peak shift to the higher binding energy, and peaks were gradually broadened. It may be related to the existing impurities in $V_{0.3}$ETS-10 upon increased vanadium incorporation. Moreover, the broadening of the O 1s peak can be an indication of some disturbed linkages or the interruption of -Ti-O-Ti- chains.

The XPS analyses presented in Fig. 5c allowed the exploration of different chemical states of vanadium (V^{4+} and V^{5+}) in the structure of V-incorporated samples. The dotted lines represent the original XPS data, while the straight lines represent the deconvoluted data. The results showed that, as the vanadium doping level increased, the area of V^{4+} decreased from 55.84 % to 32.76 %, while the area of V^{5+} increased from 44.61 % to 67.23 %. These results suggested that vanadium exists in two different oxidation states in the structure with a more significant amount of V^{5+} as the vanadium doping level increased.

UV–vis spectroscopic analysis was conducted to determine the effect of vanadium incorporation on the bandgap of the ETS-10 sample. The UV-Vis spectra and the corresponding Tauc plot of the samples are shown in Fig. 6. The inset of Fig. 6a presents the UV-Vis plot of absorption in the 200–800 nm region.

The UV–vis absorption spectra of ETS-10 and V-incorporated ETS-10 samples demonstrated a strong absorption band in the 250–300 nm

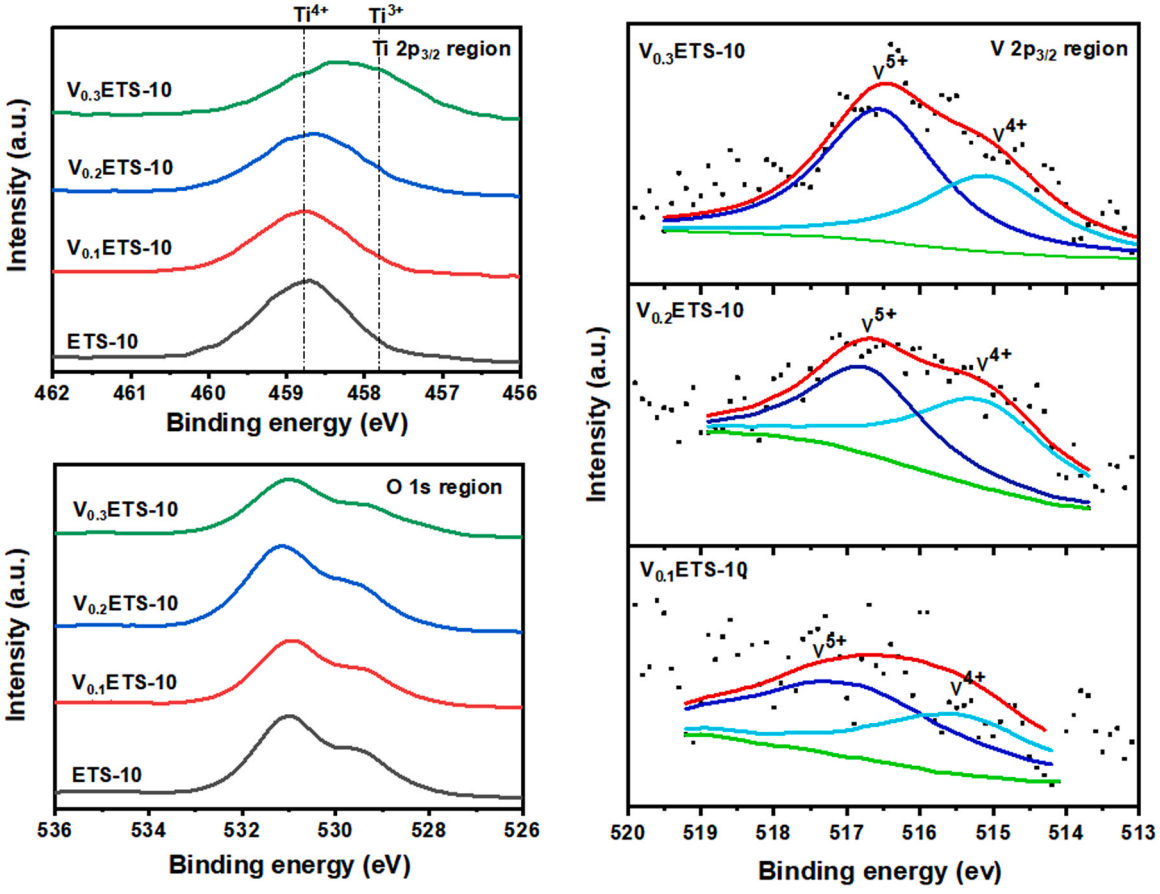


Fig. 5. XPS spectra of (a) Ti $2p_{3/2}$, (b) O 1 s, and (c) V $2p_{3/2}$ binding energies of ETS-10.

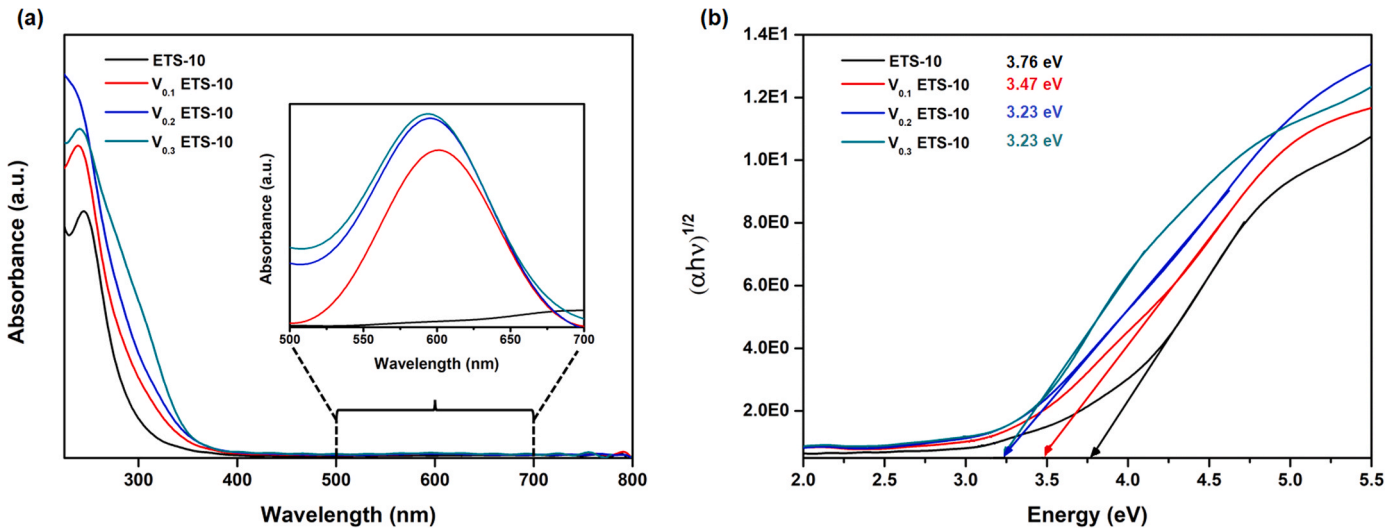


Fig. 6. UV–vis absorption spectra (a) and Tauc plot (b) of ETS-10 and vanadium-substituted ETS-10 samples.

region corresponding to different components of O^{2-} to Ti^{4+} charge-transfer transitions along the -Ti-O-Ti- chains [34] The $V_{0.3}$ETS-10 sample showed the maximum blue-shift in the absorption band from ~244 nm to 225 nm, which may be attributed to increased defect formation in the -Ti-O-Ti- chains upon vanadium incorporation. Additionally, the absorption band indicating the delocalized charge-transfer transition became broader in the V-incorporated samples, suggesting more interrupted chains than the unmodified sample [35]. Moreover, a new absorption at ~600 nm corresponding to metal-to-metal transitions with V^{4+} was observed, indicating the substitution of V for Ti in ETS-10 [21,34].

The corresponding bandgap values were determined from the Tauc plots, as shown in Fig. 6b. The bandgap energy values were calculated as 3.76 eV for ETS-10, which were in correlation with what was observed in the literature [31]. Upon incorporation of vanadium, this value decreased to 3.47 eV for $V_{0.1}$ETS-10 and 3.23 eV for $V_{0.2}$ETS-10 and $V_{0.3}$ETS-10 samples. Accordingly, the incorporation of vanadium into the structure of ETS-10 appears to result in decreased bandgap values compared to the unmodified ETS-10 sample. The decreased bandgap, in addition to the presence of V^{5+} cations, was shown to indicate that the vanadium incorporation induces new low optical energy transitions into the band structure, creating localized mid-gap states [36]. The presence of V^{5+} cations was additionally shown to potentially induce structural changes in the -Ti-O-Ti- wire geometry, leading to an improvement in photocatalytic performance [21]. However, beyond a certain optimal concentration, these sites acted as recombination centers reducing the overall photocatalytic activity [22].

3.2. Humidity sensing performances

Fig. 7a–d shows the impedance response characteristics of all sensors as a function of relative humidity (*RH)* at the frequency of 100 Hz, which was identified as the optimal frequency for humidity measurements. Table 2 provides the sensitivity (*S*), which is $S=Im_{8\%RH}/Im_{97\%RH}$, and linearity (R^2) values for all sensors across the full (*Full range*) and low *RH* range (*LRH*). While the $V_{0.2}$ETS-10 sample exhibited the maximum sensitivity ($S_{full\ range}$) and the best fit (R^2=0.9914), it is noteworthy that all samples displayed a variation spanning more than three to four orders of magnitude across the entire *RH* range (8 % to 97 %) indicating an overall high sensitivity in ETS-10 based titanosilicates to changes in humidity. These results indicate that the ETS-10 and V-incorporated ETS-10 films deposited on quartz glass substrates hold significant promise for humidity sensing applications.

Compared to the ETS-10, $V_{0.1}$ETS-10, and $V_{0.3}$ETS-10 samples, a significant improvement in the performance was observed in the low *RH* region *(LRH<32%)* for the $V_{0.2}$ETS-10 sensor. To facilitate a precise comparison of the low *RH* region with the medium and high *RH* ranges, the R^2 and sensitivity data are presented separately in Fig. 7e–f. The results summarized in Table 2 as S_{LRH} ($S_{LRH}=Im_{8\%RH}/Im_{32\%RH}$), and R^2_{LRH} reveal a substantial performance enhancement in the $V_{0.2}$ETS-10 sensor with an R^2_{LRH} value of 0.9980.

On the other hand, as the vanadium content was further increased in the $V_{0.3}$ETS-10 sample, a noticeable decrease in sensitivity at the low *RH* region was observed. These findings suggest that increasing the vanadium content to an optimized level led to enhanced sensor sensitivity at low *RH* levels (<32 % *RH*). Notably, no significant change was observed at medium and high *RH* levels. Therefore, it can be concluded that V-incorporated ETS-10 sensors with an optimized vanadium content exhibited enhanced sensitivity for humidity sensing, particularly at low *RH* values, representing a novel advancement in this field.

Based on these results in Table 2, the V-incorporated ETS-10 sensor were compared with other sensing materials based on TiO_2 in the literature, as shown in Table 3. The sensitivity is defined as $S=Im_{a\%RH}/Im_{b\%RH}$ (where a is the lowest relative humidity measured, and b is the highest relative humidity measured) found to be highly linear. It can be particularly inferred that in comparison with other V-doped TiO_2 sensors, the $V_{0.2}$ETS-10 developed in this work with optimized vanadium content is highly sensitive and linear throughout the whole range. However, a quantitative comparison in terms of linearity could not be made in Table 3, since the references mentioned lack linearity data.

Additionally, the response and recovery times of $V_{0.2}$ETS-10 are significantly shorter than the reported TiO_2 sensors.

The observed enhancement in sensitivity, in comparison with unmodified ETS-10, can be attributed to the introduction of new states upon vanadium incorporation as confirmed by Raman and XPS spectroscopy measurements. Our observations indicate that Ti^{4+} ions in the original ETS-10 structure existing in the -Ti-O-Ti- wires were chemically reduced to Ti^{3+} due to vanadium incorporation as evidenced by XPS results (see Fig. 4). With an optimized amount of vanadium doping ($V_{0.2}$ETS-10), the formation of Ti^{3+} could result in higher electron density [37,38]. In accordance with the XPS findings, this mechanism coincides with the emergence of V^{4+} and V^{5+} states in the -Ti-O-Ti- wire. Due to the unstable nature of V^{5+}, these ions act as water dissociation sites even at low *RH* levels (8 %–32 %). A similar doping mechanism was used to attribute V^{5+} sites generating hydroxyl groups (V-OH sites) on the surface, leading to enhanced photocatalytic activity [22]. However, beyond some optimal concentration of incorporated vanadium, i.

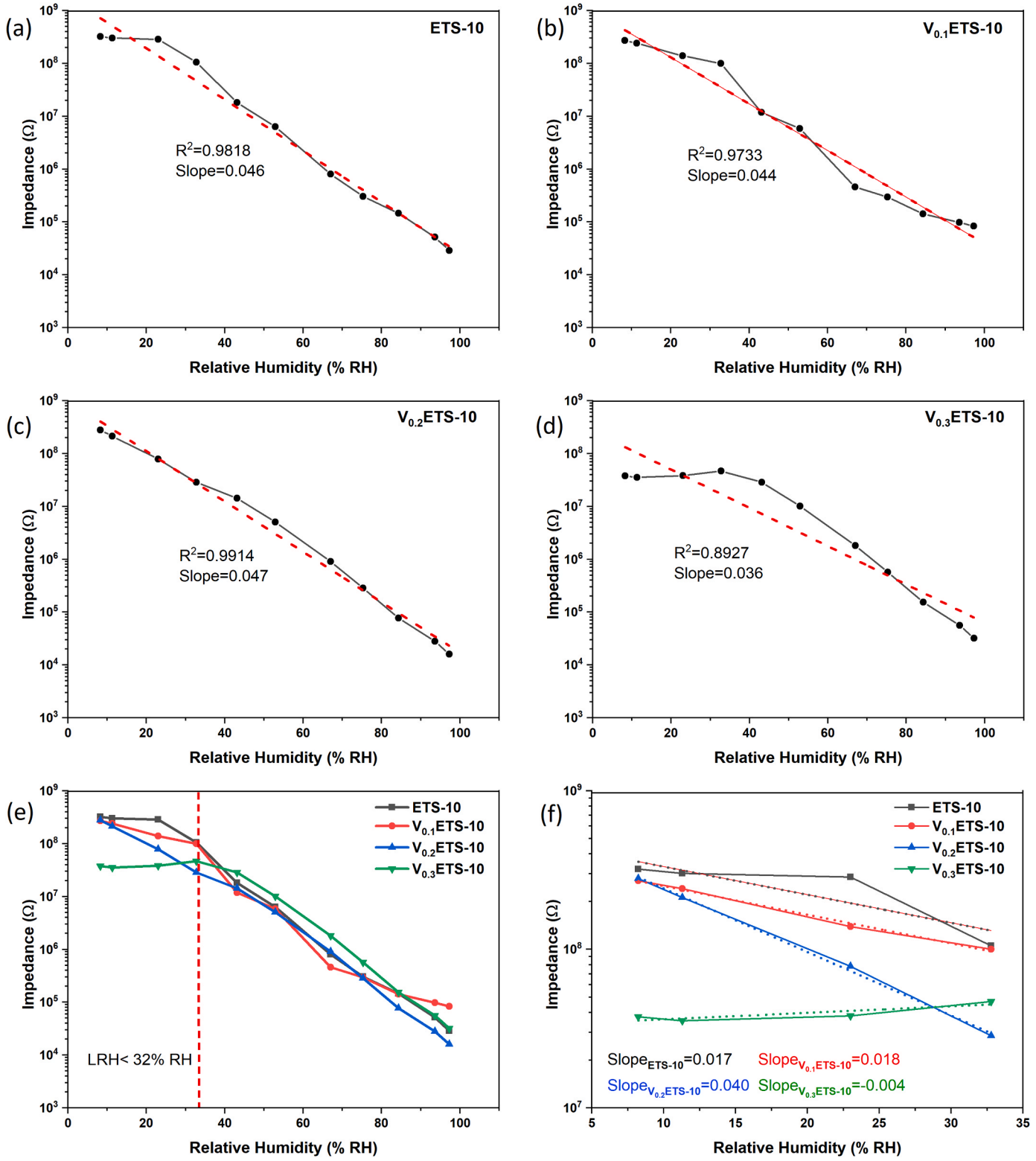


Fig. 7. Relationship between impedance modulus and % *RH* for ETS-10 (a), $V_{0.1}$ETS-10 (b), $V_{0.2}$-ETS-10 (c), $V_{0.3}$-ETS-10 (d), for all sensors at a frequency of 100 Hz at whole relative humidity range (e), and at Low relative humidity range (f).

e., $V_{0.3}$ETS-10, humidity sensing performance declines at low *RH* values. This decrease in sensitivity may be attributed to the increased number of V^{5+} sites in the -Ti-O-Ti- chain, which is believed to lead to the formation of longer -V^{5+}-O-V^{5+} chains, as evident in the Raman spectra. It is plausible that, at higher vanadium content, some vanadium moieties adopt the form of vanadium oxide, giving rise to energetically unfavorable chains indicating an unstable ETS-10 structure [21].

Furthermore, the $V_{0.3}$ETS-10 sample exhibited impurities such as quartz and anatase phases within the structure upon increased vanadium incorporation, as evidenced by XRD results (Fig. 2). This emergence of new phases with increased vanadium content was also confirmed by observable morphological changes in the structure of the

Table 2
Sensing performance of the sensors in the operating ranges at room temperature.

Sample	$S_{full\ range}$	S_{LRH}	$R^2_{full\ range}$	R^2_{LRH}	Res/Rec
ETS-10	1.11×10^4	3. 04	0.9818	0. 6316	8/35
$V_{0.1}$ETS-10	3.25×10^3	2.71	0.9733	0.9917	8/35
$V_{0.2}$ETS-10	1.75×10^4	9.83	0.9914	0.9980	8/40
$V_{0.3}$ETS-10	1.17×10^3	0. 81	0.8927	0.7551	8/40

Table 3
The performance comparison of V-incorporated ETS-10 with various humidity sensing materials.

Materials type	Response/ recovery	Sensitivity	Humidity range (%)
V-doped TiO_2 Nanorods Array[15]	660/500	15	40–90
V-doped TiO_2 3D[14]	~150/400	314	40–90
V-doped TiO_2:WO_3[16]	–	10	30–100
Ordered mesoporous Co-doped TiO_2[13]	24/400	$\sim 1.39 \times 10^5$	9–90
TiO_2 modified with GO[11]	28/500	$\sim 10^6$	9–90
$V_{0.2}$ETS-10 (this study)	8/40	$\sim 1.75 \times 10^4$	8–97

films, as revealed in the SEM results (Fig. 3). Consequently, exceeding the optimal vanadium level leads to a significant decrease in resistance at room temperature. Similar observations were made for Co-doped mesoporous TiO_2 resulting in low sensitivity towards humidity sensing [13].

In addition, the response and recovery time of sensors were also measured by the simultaneous change of impedance from the relative humidity values of 97 % to 32 % and vice versa (Fig. 8a). Response time, which was less than 10 s, and the recovery time, approximately 35–40 s as mentioned in Table 2, were consistent across all samples. Long-term stability tests were conducted on the $V_{0.2}$ETS-10 sensor for real-life applications. For this purpose, the sensor was placed inside a desicator with a valve connected to the room environment. Humidity-sensing performance of the samples was tested after 30, 60, 120, and 180 days to record its long-term stability. The impedance values for the $V_{0.2}$ETS-10 sensor were measured at three different *RH* levels over a 180-day period, as shown in Fig. 8b confirming the significant stability and durability of this sample.

3.3. Humidity sensing mechanism and effect of vanadium-incorporation

For a deeper insight into the humidity sensing behavior of the samples, Nyquist plots were constructed encompassing the whole humidity range as shown in Fig. 9a.

As depicted in Fig. 9a, when humidity was introduced at a very low *RH* level (11 %), only a small amount of water was adsorbed to form a chemisorbed water layer resulting in very high impedance values indicating proton hopping was very low at this stage [39]. As *RH* levels increased to 52 % and 75 %, a semicircle started to form gradually, leading to a significant decrease in impedance. It is possible that at increased *RH* levels, physisorbed water molecules constitute an uninterrupted water layer, which makes proton hopping easier, as observed upon increased conduction with the formation of complete semicircles. At these *RH* levels, a physisorbed water layer begins to form in coordination with the larger numbers of hydroxyl ions on defect sites. The subsequent adsorption of water on the hydroxyl layer forms the physically absorbed water layer, which leads to the decomposition of water molecules into hydronium ions (H_3O^+), and then H_3O^+ becomes the main carrier [40].

At high *RH* levels of 93 %, water molecules accumulate on top of each other, leading to a considerable increase in conduction originating from the proton hopping mechanism. As the conductivity increases, the resistance decreases progressively. At high *RH* levels, the semicircle becomes smaller, and a short tail appears at the end of the semicircle in the low-frequency range. At this stage, physisorbed water molecules move easily, and the proton hopping mechanism becomes the primary conduction mechanism [41]. Fig. 9b represents the equivalent circuit for the sensor at different *RH* values. The tail in Fig. 9b is represented with Z_W, corresponding to the Warburg impedance in the equivalent circuit [40].

Microporous structures are of key importance to achieve optimal performance owing to their multifaceted porous architecture comprising different levels of pore network [42]. Fig. 10 illustrates three distinct crystal regions involved in water adsorption at varying *RH* levels for the $V_{0.2}$ETS-10 sample: intracrystalline (within the ETS-10 crystalline pore network), intercrystalline (between crystal particles), and surface water.

At low *RH* levels, water molecules primarily chemisorbed within the nanopores and channels inside the zeotype crystals, as well as defective sites on the surface as depicted in Fig. 10a. At this stage, proton hopping occurs through the chemisorbed intracrystalline water, with the

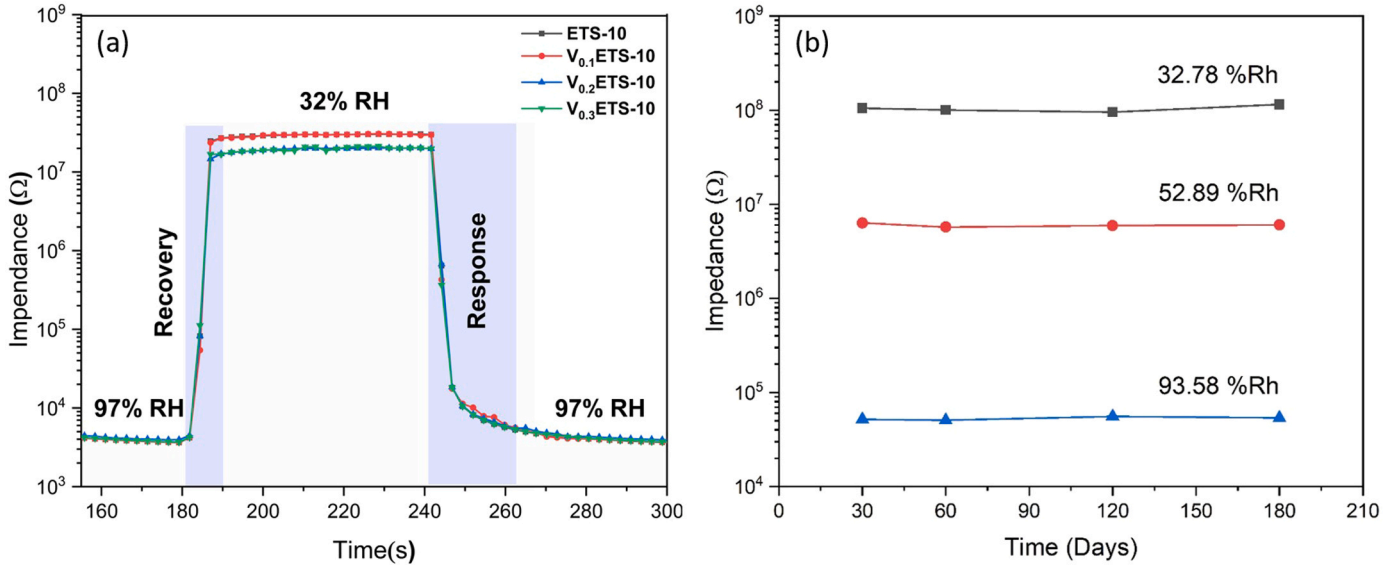


Fig. 8. The transient response dynamics of the impedance of sensors switching back and forth between 32 % and 97 % *RH* (a), Long term stability tests of $V_{0.2}$ETS-10 (b).

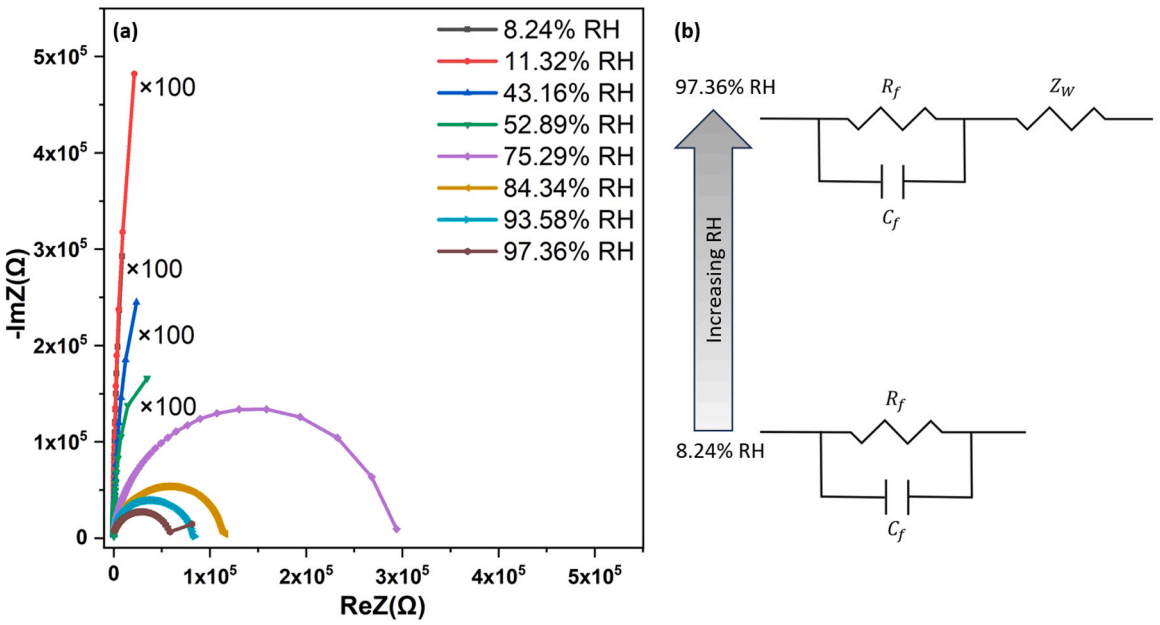


Fig. 9. Complex impedance spectra of $V_{0.2}$ETS-10 at various relative humidity values (a), Equivalent circuit of the sensors at different *RH* levels. R_f: film resistance; C_f: film capacitance; Z_W: Warburg impedance (b).

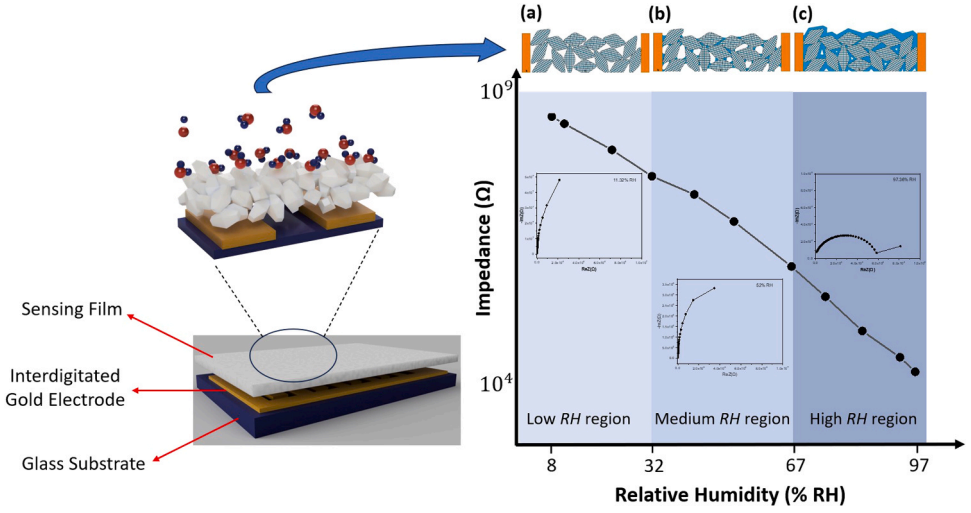


Fig. 10. Schematic view of humidity sensing behavior of $V_{0.2}$ETS-10 at low, medium, and high relative humidity (RH%) levels.

influence of defects being particularly pronounced. As *RH* levels increase (reaching medium *RH*), water condensation takes place at the grain boundaries within intercrystalline voids. Eventually, the grain surfaces become covered with water, resulting in a decrease in impedance and the formation of a semicircle (Fig. 10b). Under high *RH* conditions, the grain surfaces are covered with a very thin layer of water (Fig. 10c). At this point, we observe Warburg impedance, indicative of the role of protons originating from physisorbed water in the humidity sensing mechanism.

The enhanced sensitivity results obtained from $V_{0.2}$ETS-10 can be interpreted through the perspective of the electronic and proton conduction mechanism as follows: The semiconductive nature of Ti-based materials demonstrates a mixed-type electronic and ionic conductivity depending on the level of defects [43,44]. The formation of defects in the form of Ti^{+3} and V^{+5} has been shown to lead to a reduction in the band gap and an enhancement in the photocatalytic activity [21,43]. A similar defect formation involving Ti^{+3} and V^{+5} was also observed in the current study. This mechanism is schematically shown in Fig. 11.

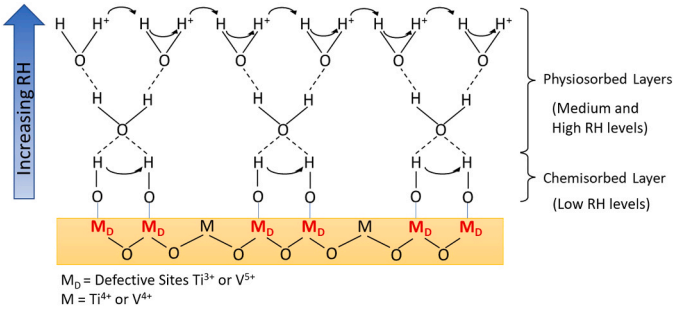


Fig. 11. The theoretical model for water adsorption on the surface of the sensor.

This defect generation results in an increase in the concentration of -OH ions with enhanced water dissociation (see Fig. 11; Md: Ti^{+3} and V^{+5}) leading to heightened chemisorption, contributing to enhanced

sensitivity at low *RH* levels. Similar results proposing the Ti^{3+} defects were also discussed for Co^{2+} to Co^{3+} oxidation by Haidry et al., suggesting that these sites can have a role in water dissociation [13]. Thus, it can be inferred that optimized incorporation of vanadium into ETS-10 offers a significant advantage for improving humidity sensing at low *RH* levels. In accordance with the XPS results, it is likely that the generation of Ti^{3+} and V^{5+} sites upon incorporating vanadium is effective on the electronic conduction mechanism at low *RH* levels governed by a reaction given in Eq.(1):

$$Ti^{4+} \leftrightarrow Ti^{3+} \quad (1)$$

$$V^{4+} \leftrightarrow V^{5+} \quad (2)$$

The high electronegativity of Ti^{+3} with respect to Ti^{+4} makes water molecules more susceptible to being adsorbed onto the surface, and the higher electron density of Ti^{+3} enhances electronic conductivity [37, 38]. The fact that optimized vanadium incorporation had a significant contribution at low *RH* levels as observed in the current study can be attributed to the proximity of V^{4+} and V^{5+} sites, which can impact overall electronic conduction [21].

In terms of the ionic conduction mechanism, water molecules are prone to be chemisorbed on defective sites, such as Ti^{+3} and V^{+5} groups, when they contact the surface of the sensor at low *RH*. Upon chemisorption, the dissociation of H_2O to H^+ and OH^- ions occurs on such defective sites represented by M_D (Fig. 11), creating the hydroxyl groups (Ti-OH, V-OH) [45]. The proton hopping mechanism occurs following the dissociation of water molecules. Mobile protons contribute to the proton hopping mechanism between the chemisorbed hydroxyl groups to impart conductivity. As the incorporated vanadium amount increases, the concentration of these defective sites increases, making proton hopping easier due to the higher amount of water dissociative sites. This phenomenon enhances conduction, specifically at low *RH* levels, where the water molecules are predominantly adsorbed by chemisorption.

The results of our study indicate that the optimized level of vanadium incorporation ($V_{0.2}$ETS-10) can enhance the sensitivity of the sensor towards low humidity levels due to electronic conductivity and proton hopping mechanisms. These mechanisms are governed by the chemisorbed water layer within the intra-crystalline channels at low *RH* levels catalyzed by the formation of defective Ti^{3+} and V^{5+} sites. As the *RH* increases, water molecules are more likely to be adsorbed in the inter-crystalline voids and on the crystal surface by physisorption, and the charge transfer is now governed by the Grotthuss chain mechanism, where the proton is released from H_3O^+ to neighboring water molecule: $H_2O + H_3O^+ = H_3O^+ + H_2O$ [41]. At higher *RH* levels, the number of defects created on the initial layer seems to have less impact on the sensitivity of sensors incorporating vanadium (V). Additionally, increasing the vanadium content above an optimized level ($V_{0.3}$ETS-10) led to notable changes in morphology, shifting from the typical bi-pyramidal shape to cubic-like structures, and an increase in impurities such as anatase and quartz, as confirmed by XRD (Fig. 2) and FE-SEM (Fig. 3) analysis. These structural alterations and the presence of impurities potentially affect vanadium clustering or introduce structural instability at higher levels of vanadium, consequently influencing its sensing behavior [30].

4. Conclusion

We have demonstrated the successful development of humidity sensors based on films prepared by using directly synthesized V-incorporated ETS-10 powder, which exhibits enhanced sensitivity and linearity across a wide range of *RH* levels. The obtained experimental results showed that maximum sensitivity was obtained in $V_{0.2}$ETS-10 with newly formed defect sites and altered local environment of the -Ti-O-Ti- wires, whereas indications of excessive vanadium incorporation occurred in $V_{0.3}$ETS-10. These results indicate that an optimized vanadium content was necessary for obtaining good performance in all *RH* levels, with particular enhancement at low *RH* (<32 % *RH*).

The observed enhancement in sensitivity upon vanadium incorporation can be attributed to several factors, primarily the reduction of Ti^{4+} ions to Ti^{+3} and the emergence of new states such as V^{5+} in the -Ti-O-Ti- wire. These defects play a crucial role in enhancing water dissociation, leading to heightened chemisorption, particularly evident at lower relative humidity (*RH)* levels. At this stage, the chemisorbed water layer within the intracrytalline voids and channels governs the humidity mechanism, transitioning to physisorbed water in the intercrytalline spaces and on the crystal surface as *RH* levels increase. Interestingly, as *RH* levels further rise, the influence of defect generation on the initial layer appears to diminish in its impact on the sensitivity of sensors incorporating vanadium (V).

These results highlight the potential of the proposed approach of direct synthesis of V-incorporated ETS-10 materials as a low humidity sensor with a very good response over a wide humidity range. Overall, our study provides insight into the relationship between vanadium content, structural changes, and humidity-sensing behavior of titanosilicate-based sensors.

CRediT authorship contribution statement

Davoudnezhad Ramona: Conceptualization, Data curation, Formal analysis, Investigation, Methodology, Validation, Visualization, Writing – original draft, Writing – review & editing. **Kuzyaka Duygu:** Conceptualization, Writing – original draft, Writing – review & editing. **Akata Burcu:** Conceptualization, Funding acquisition, Project administration, Supervision, Writing – original draft, Writing – review & editing.

Data Availability

Data will be made available on request.

Acknowledgements

This study was supported by a TUBITAK project, “Production and Improvement of Humidity Sensors from Microporous Titanosilicate and Vanadosilicate Thin Films,” with project number 118M631. The support provided by METU-Central Laboratory is greatly acknowledged.

References

[1] N. Yamazoe, Toward innovations of gas sensor technology, Sens. Actuators B Chem. (2005) 2–14, https://doi.org/10.1016/j.snb.2004.12.075.
[2] D. Nunes, A. Pimentel, A. Goncalves, S. Pereira, R. Branquinho, P. Barquinha, E. Fortunato, R. Martins, Metal oxide nanostructures for sensor applications, Semicond. Sci. Technol. 34 (2019), https://doi.org/10.1088/1361-6641/ab011e.
[3] K.G. Krishna, S. Parne, N. Pothukanuri, V. Kathirvelu, S. Gandi, D. Joshi, Nanostructured metal oxide semiconductor-based gas sensors: a comprehensive review, Sens. Actuators A Phys. 341 (2022), https://doi.org/10.1016/j.sna.2022.113578.
[4] Z. Ma, T. Fei, T. Zhang, An overview: sensors for low humidity detection, Sens. Actuators B Chem. 376 (2023), https://doi.org/10.1016/j.snb.2022.133039.
[5] H. Wang, Q. Gao, H. Li, H. Wang, One-step template-free synthesis of Mn(II)-doped TiO2 hierarchical microspheres with unique radiating fibrous structure for efficient Fenton degradation, Mater. Res Bull. 118 (2019), https://doi.org/10.1016/j.materresbull.2019.110508.
[6] X. Tong, W. Shen, X. Chen, Enhanced H 2 S sensing performance of cobalt doped free-standing TiO 2 nanotube array film and theoretical simulation based on density functional theory, Appl. Surf. Sci. 469 (2019) 414–422, https://doi.org/10.1016/j.apsusc.2018.11.032.
[7] M.M. Momeni, M. Hakimian, A. Kazempour, In-situ manganese doping of TiO2 nanostructures via single-step electrochemical anodizing of titanium in an electrolyte containing potassium permanganate: a good visible-light photocatalyst, Ceram. Int. 41 (2015) 13692–13701, https://doi.org/10.1016/j.ceramint.2015.07.158.
[8] H. Farahani, R. Wagiran, M.N. Hamidon, Humidity sensors principle, mechanism, and fabrication technologies: A comprehensive review, 2014. ⟨https://doi.org/10.3390/s140507881⟩.
[9] Z. Chen, C. Lu, Humidity sensors: a review of materials and mechanisms, Sens. Lett. 3 (2005) 274–295, https://doi.org/10.1166/sl.2005.045.

[10] A.I. Buvailo, Y. Xing, J. Hines, N. Dollahon, E. Borguet, TiO 2/LiCl-based nanostructured thin film for humidity sensor applications, ACS Appl. Mater. Interfaces 3 (2011) 528–533, https://doi.org/10.1021/am1011035.
[11] L. Sun, A.A. Haidry, Q. Fatima, Z. Li, Z. Yao, Improving the humidity sensing below 30% RH of TiO2 with GO modification, Mater. Res. Bull. 99 (2018) 124–131, https://doi.org/10.1016/j.materresbull.2017.11.001.
[12] A.A. Haidry, Q. Fatima, Z. Wang, Y. Wang, Y. Ji, A. Raza, Optimization of the specific surface area of ordered mesoporous TiO2 yields a high response to humidity, Colloids Surf. A Physicochem. Eng. Asp. 667 (2023), https://doi.org/10.1016/j.colsurfa.2023.131371.
[13] Z. Li, A.A. Haidry, B. Gao, T. Wang, Z.J. Yao, The effect of Co-doping on the humidity sensing properties of ordered mesoporous TiO 2, Appl. Surf. Sci. 412 (2017) 638–647, https://doi.org/10.1016/j.apsusc.2017.03.156.
[14] M.Z. Musa, M.H. Mamat, N. Vasimalai, I.B. Shameem Banu, N. Parimon, H. Hassan, M.F. Malek, M. Rusop, Humidity sensing performance of V: TiO23D nanostructure-based humidity sensor. IOP Conf Ser Earth Environ Sci, IOP Publishing Ltd,, 2021. ⟨https://doi.org/10.1088/1755-1315/682/1/012073⟩.
[15] M.Z. Musa, M.H. Mamat, M.A. Othman, I.B. Shameem, N. Vasimalai, M.F. Malek, M. Rusop, Enhanced sensitivity of humidity sensor prepared using vertically aligned V-doped TiO2 nanorods array, J. Electr. Electron. Syst. Res. (2020) 68–73.
[16] P.M. Faia, J. Libardi, C.S. Louro, Effect of V2O5 doping on p- to n-conduction type transition of TiO2:WO3 composite humidity sensors, Sens. Actuators B Chem. 222 (2016) 952–964, https://doi.org/10.1016/j.snb.2015.09.039.
[17] H. Aoki, Y. Azuma, T. Asaka, M. Higuchi, K. Asaga, K. Katayama, Improvement of response characteristics of TiO2 humidity sensors by simultaneous addition of Li2O and V2O5, Ceram. Int. 34 (2008) 819–822, https://doi.org/10.1016/j.ceramint.2007.09.030.
[18] R. Grau-Crespo, U. Schwingenschlögl, The interplay between dopants and oxygen vacancies in the magnetism of V-doped TiO2, J. Phys. Condens. Matter 23 (2011), https://doi.org/10.1088/0953-8984/23/33/334216.
[19] N.C. Jeong, M.H. Lee, K.B. Yoon, Length-dependent band-gap shift of TiO32- molecular wires embedded in zeolite ETS-10, Angew. Chem. - Int. Ed. 46 (2007) 5868–5872, https://doi.org/10.1002/anie.200701676.
[20] C.J. Nak, J.L. Young, J.H. Park, H. Lim, C.H. Shin, H. Cheong, B.Y. Kyung, New insights into ETS-10 and titanate quantum wire: a comprehensive characterization, J. Am. Chem. Soc. 131 (2009) 13080–13092, https://doi.org/10.1021/ja903638v.
[21] A.M. Shough, D.J. Doren, M. Nash, R.F. Lobo, Effects of vanadium substitution on the structure and photocatalytic behavior of ETS-10, J. Phys. Chem. C 111 (2007) 1776–1782, https://doi.org/10.1021/jp0662247.
[22] M.J. Nash, S. Rykov, R.F. Lobo, D.J. Doren, I. Wachs, Photocatalytic Activity of Vanadium-Substituted ETS-10, (2007). ⟨https://doi.org/10.1021/jp067259⟩.
[23] E.P. Ng, S. Mintova, Nanoporous materials with enhanced hydrophilicity and high water sorption capacity, Microporous Mesoporous Mater. 114 (2008) 1–26, https://doi.org/10.1016/j.micromeso.2007.12.022.
[24] Z. Li, M. Zhang, L. Yang, R. Wu, Z. Wu, Y. Jiang, L. Zhou, Y. Liu, The effect of surface hydroxyls on the humidity-sensitive properties of LiCl-doped ZnSn(OH)6 sphere-based sensors, Nanomaterials 12 (2022), https://doi.org/10.3390/nano12030467.
[25] L. Lv, F. Su, X.S. Zhao, A reinforced study on the synthesis of microporous titanosilicate ETS-10, Microporous Mesoporous Mater. 76 (2004) 113–122, https://doi.org/10.1016/j.micromeso.2004.08.004.
[26] M.N. Ismail, Hydrothermal synthesis and characterization of titanosilicate ETS-10: preparation for research integrated inorganic chemistry laboratory course, J. Chem. Educ. 97 (2020) 1588–1594, https://doi.org/10.1021/acs.jchemed.0c00165.
[27] Z. Ji, J. Warzywoda, A. Sacco, Competitive nucleation and growth in seeded batch crystallization of titanosilicate ETS-10 using Ti(SO4)2, Microporous Mesoporous Mater. 81 (2005) 201–210, https://doi.org/10.1016/j.micromeso.2005.01.029.
[28] S.J. Datta, K.B. Yoon, Synthesis of large monodisperse ETS-10 crystals and observation of quantum confinement effects from very long titanate quantum wires, Catal. Today 204 (2013) 60–65, https://doi.org/10.1016/j.cattod.2012.08.006.
[29] S.J. Datta, K.B. Yoon, Length-dependent change of optical, magnetic, and vibrational properties of vanadate (V IVO 32-) quantum wire embedded in AM-6 vanadosilicate, J. Am. Chem. Soc. 134 (2012) 17202–17211, https://doi.org/10.1021/ja307187z.
[30] J.H. Yu, S.H. Nam, J.W. Lee, D.I. Kim, J.H. Boo, Oxidation state and structural studies of vanadium-doped titania particles for the visible light-driven photocatalytic activity, Appl. Surf. Sci. 472 (2019) 46–53, https://doi.org/10.1016/j.apsusc.2018.04.125.
[31] S. Bordiga, G.T. Palomino, A. Zecchina, G. Ranghino, E. Giamello, C. Lamberti, Stoichiometric and sodium-doped titanium silicate molecular sieve containing atomically defined -OTiOTiO- chains: quantum ab initio calculations, spectroscopic properties, and reactivity, J. Chem. Phys. 112 (2000) 3859–3867, https://doi.org/10.1063/1.480533.
[32] Y. Wang, D.J. Doren, Electronic structures of V-doped anatase TiO2, Solid State Commun. 136 (2005) 142–146, https://doi.org/10.1016/j.ssc.2005.07.014.
[33] H. Liu, F. Shen, M. Xing, J. Zhang, M. Anpo, Synthesis, characterization and photoactivity of vacuum activated V 4+ and Ti3+ doped TiO2, Catal. Lett. 144 (2014) 1494–1498, https://doi.org/10.1007/s10562-014-1308-3.
[34] Z. Ji, M.N. Ismail, D.M. Callahan, J. Warzywoda, A. Sacco, Transition metal ion substitution in titanosilicate ETS-10 for enhanced UV light photodegradation of methylene blue, J. Photochem. Photobiol. A Chem. 221 (2011) 77–83, https://doi.org/10.1016/j.jphotochem.2011.04.027.
[35] B. Yilmaz, J. Warzywoda, A. Sacco, Spectroscopic characterization of the quantum wires in titanosilicates ETS-4 and ETS-10, Nanotechnology 17 (2006) 4092–4099, https://doi.org/10.1088/0957-4484/17/16/017.
[36] A. Marie Shough, R.F. Lobo, D.J. Doren, A visible light photocatalyst: effects of vanadium substitution on ETS-10, Phys. Chem. Chem. Phys. 9 (2007) 5096–5104, https://doi.org/10.1039/b703187d.
[37] T. Song, S. Ye, H. Liu, Y.G. Wang, Self-doping of Ti3+into Na2Ti3O7 increases both ion and electron conductivity as a high-performance anode material for sodium-ion batteries, J. Alloys Compd. 767 (2018) 820–828, https://doi.org/10.1016/j.jallcom.2018.07.186.
[38] G. Yang, S.J. Park, The formation mechanism of Li 4 Ti 5 O 12−y solid solutions prepared by carbothermal reduction and the effect of Ti 3+ on electrochemical performance, Sci. Rep. 9 (2019), https://doi.org/10.1038/s41598-019-41206-0.
[39] C. Yang, H. Zhang, W. Gu, C. Chen, Preparation and mechanism investigation of highly sensitive humidity sensor based on Ag/TiO2, Curr. Appl. Phys. 43 (2022) 57–65, https://doi.org/10.1016/j.cap.2022.08.006.
[40] M. Mekawy, H. Noguchi, J. Kawakita, Quantitative and qualitative studies for real monitoring of interfacial molecular water, J. Colloid Interface Sci. 613 (2022) 311–319, https://doi.org/10.1016/j.jcis.2022.01.025.
[41] N. Agmon, The Grotthuss mechanism, Chem. Phys. Lett. 244 (1995) 456–462, https://doi.org/10.1016/0009-2614(95)00905-J.
[42] L.H. Chen, M.H. Sun, Z. Wang, W. Yang, Z. Xie, B.L. Su, Hierarchically structured zeolites: from design to application, Chem. Rev. 120 (2020) 11194–11294, https://doi.org/10.1021/acs.chemrev.0c00016.
[43] Y.K. Krisnandi, R.F. Howe, Effects of ion-exchange on the photoreactivity of ETS-10, Appl. Catal. A Gen. 307 (2006) 62–69, https://doi.org/10.1016/j.apcata.2006.03.008.
[44] S. Galioglu, I. Cam, B. Akata, Ionic conductivity of microporous titanosilicate ETS-10 and ion-exchanged Mn+-ETS-10 (where, Mn+ = Li+, Na+, Mg2+, Zn2+, Ca2+) thin films prepared by secondary growth method, Microporous Mesoporous Mater. 250 (2017) 177–185, https://doi.org/10.1016/j.micromeso.2017.05.018.
[45] S.J. Datta, K.B. Yoon, Synthesis of ideal AM-6 and elucidation of v4+-to-O charge transfer in vanadate quantum wires, Angew. Chem. - Int. Ed. 49 (2010) 4971–4975, https://doi.org/10.1002/anie.200907088.



Dr. Ramona Davoudnezhad gained her Ph.D. in the Micro and Nanotechnology Department, METU, in 2022. Her research areas are synthesis, characterization, and thin-film applications of zeolites, zeo-type materials, and MOFs. Besides, she focused on the humidity-sensing applications of these materials. Currently, she has been working as a senior researcher in the Mechanical Engineering Department at Middle East Technical University (METU).



Dr. Duygu Kuzyaka completed her Ph.D. in the Micro and Nanotechnology Department at METU in 2019. During her Ph. D. studies, she worked on zeolite and zeo-type materials, thin-film production, photocatalysis, defect formation in thin films, and advanced characterization techniques. Currently, she is a senior researcher at the Center for Solar Energy Research and Applications (ODTÜ – GÜNAM).



Prof. Dr. Burcu Akata received her Ph.D. in chemical engineering, and she is currently a professor in the Micro and Nanotechnology Department at Middle East Technical University (METU). Her research is focused on nanoporous materials in powder and thin film forms for obtaining enhanced behavior in advanced applications. These activities can be summarized as sensors and biosensors, photocatalysis, and MOFs for energy storage applications. Additionally, she is working closely with industries to scale up a solar thermal process to synthesize industrial zeolites from raw natural minerals.